analytical chemistry

pubs.acs.org/ac Article

Noninvasive Skin Respiration (CO_2) Measurement Based on Quartz-Enhanced Photoacoustic Spectroscopy

Biao Li,[§] Hongpeng Wu,[§] Chaofan Feng, Suotang Jia, and Lei Dong*

Cite This: *Anal. Chem.* 2023, 95, 6138−6144 Read Online

ACCESS | Metrics & More | Article Recommendations

ABSTRACT: A noninvasive method for disease diagnosis that does not require complex specialized laboratory facilities and chemical reagents is particularly attractive in the current medical environment. Here, we develop a noninvasive skin respiration sensor based on quartz-enhanced photoacoustic spectroscopy (QEPAS) that can monitor the skin elimination rate of carbon dioxide (CO_2). A 3.8 mW distributed feedback laser emitting at 2.0 μm is used as an excitation source, and a three-dimensional (3D)-printed acoustic detection module is designed to apply to the skin as a sensor head. The performance of the noninvasive skin respiration sensor is assessed in terms of detection sensitivity, linearity, long-term stability, and water effect. A minimum detection limit of 35 ppb is achieved at the optimal integration time of 670 s. The skin respiration measurements from eight healthy volunteers are recorded, and the real-time results are analyzed.

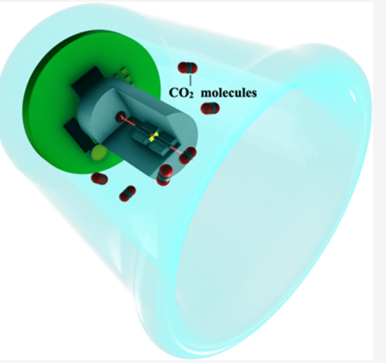

INTRODUCTION

Medical professionals have been increasingly focusing attention on noninvasive diagnoses in recent years. For disease screening, noninvasive measurements of biological gas concentrations are a convenient and safe solution.[1−4] Skin gas monitoring and exhaled breath analysis are both excellent noninvasive diagnostic procedures. Carbon dioxide (CO_2), a product of cellular metabolism, plays a very important role in the diagnosis of human health. Gerlach first proposed skin breathing,[5] which demonstrated that the skin of the human body eliminates carbon dioxide. During their research, it was found that the CO_2 eliminated from the skin is due to the metabolism of blood vessels and cells. And a device for detecting skin respiration was reported.[6] However, even though this method can obtain the required information, it has disadvantages in terms of its large volume and the need to change samples frequently. Skin CO_2 monitoring has been used to assess newborns' blood gas levels and reduce punctures, thus preventing hypercapnia and hypocapnia from posing a threat to their health in the past few decades.[7−10] Furthermore, this method has also been applied to critically ill patients, where it is possible to get insight into sudden changes in the condition of critically ill patients and ensure their early rescue. The current clinical device used to measure skin CO_2 is the transcutaneous monitor (TCM). This device works based on electrochemical principles and can obtain CO_2 data in a noninvasive, real-time manner. However, due to its mechanism, the TCM, which is based on electrochemical principles,[11,12] must be recalibrated every 4−6 h. Sensor electrodes and measurement locations need to be changed every 4 h, and measurements can be affected by water vapor. It is for this reason that a better method is needed. So far, a variety of methods have been studied to overcome the limitations of current skin gas monitoring methods, such as optical sensors based on fluorescence and phosphorescence.[13−15] Nonetheless, the ideal method of clinical monitoring should be noninvasive, reliable, rapid, reproducible, and intuitive. Until now, the demand for a highly sensitive, fast-response, gas-selective, portable skin gas sensor that can operate continuously has remained strong.

It has been noted that, since the advent of photoacoustic spectroscopy (PAS), there has been a steady increase in the number of photoacoustic gas sensing techniques reported, of which the trace-gas sensor based on quartz-enhanced photoacoustic spectroscopy (QEPAS) is a promising candidate for skin gas analysis due to its high immunity against environmental acoustic noise and its ability to analyze samples as small as 1 mm^3.[16] As opposed to conventional microphones, the QEPAS-based sensor employs a quartz tuning fork (QTF) as a resonant acoustic transducer to detect a weak acoustic wave caused by optical radiation interacting with a trace gas.[17−30] This paper proposes a sensor based on the QEPAS technique

Received: February 5, 2023
Accepted: March 22, 2023
Published: March 29, 2023

https://doi.org/10.1021/acs.analchem.3c00536
Anal. Chem. 2023, 95, 6138−6144

for quantitative online analysis of CO_2 eliminated from the skin.

EXPERIMENTS

Design of Skin Respiration QEPAS Sensor. Due to the action of a specific-wavelength laser, CO_2 gas molecules transition from a low-energy state to a high-excitation state. Then, a nonradiative transition occurs, and the energy released in the collision is converted into intramolecular energy, causing the local temperature of the gas molecules to rise. Periodic changes in the temperature cause the volume of the gas to expand and contract, which in turn generates sound waves. The sound waves drive the QTF to vibrate, and the concentration of CO_2 gas is inverted by the QTF into the electrical signal. An optical skin sensor head (SSH) with a sampling area of 8.5 cm^2 was prepared (Figure 1). The SSH

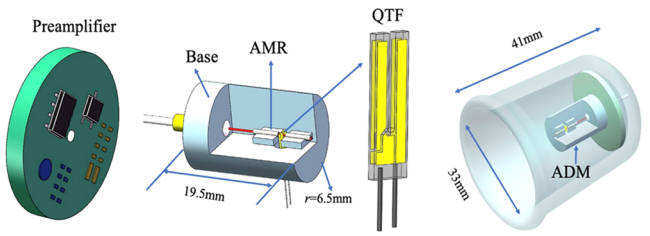

Figure 1. Schematic illustration of the skin sensor head based on QEPAS. AMR: acoustic micro-resonators. QTF: quartz tuning fork.

comprises a cover, an acoustic detection module (ADM), and a preamplifier. The transparent silicone cover can adhere to the skin and prevent ADM gas exchange with the external environment. The QEPAS-based ADM was designed, including a base, a QTF, a pair of acoustic micro-resonators (AMR), and a fiber collimator. The ADM base was 3D-printed using photosensitive resin. The ADM used a commercially available standard QTF with a resonance frequency of 32.76 kHz. The length, width, and gap of the QTF prongs are 7.5, 1.5, and 0.3 mm, respectively. The two AMRs were added on both sides of the QTF, which has been positioned 0.5 mm from each side of the QTF and 0.7 mm from the top, serving as an energy collector. The parameters of this AMR have been determined to be optimal.[31] The fiber collimator, AMR, and QTF are precisely bonded together on the ADM base by the epoxy structural adhesive so that the emitted laser beam passes perfectly through the prong gap without touching any obstacles. When gas molecules absorb the modulated laser beam, the sound waves produced will be amplified by the two AMRs. As a result of the interaction between the QTF and the AMRs,[31] the vibration amplitude of the QTF prongs increases, and the performance of the ADM is improved. The ADM was finally integrated with a homemade preamplifier, which allowed the device to be more portable.

Selection of Absorption Lines and Establishment of the Sensing System. The selection of gas absorption lines is essential for highly sensitive and selective detection. There are usually two factors to consider: the first is a commercially available laser source, and the second is the appropriate absorption line strength to meet detection sensitivity requirements and avoid interference from other absorption lines. Near-infrared distributed feedback (DFB) lasers can target the CO_2 overtone bands at 1.57 μm. However, the near-infrared absorption line strengths of CO_2 are not sufficient for the detection of skin respiration. Mid-infrared quantum cascade lasers (QCLs) and interband cascade lasers (ICLs) can offer ppb-level CO_2 detection sensitivity at 4.25 μm, where the absorption line strength is 3−4 orders of magnitude larger than those in the near-infrared overtone bands. However, mid-infrared laser sources have large sizes, high costs, and strict requirements for heat dissipation. Therefore, it is of interest to detect skin respiration using the 20012-00001 overtone bands in the 2.0 μm wavelength region, which provides a compromise between detection sensitivity, cost, and reliability. A continuous-wave 2.0 μm laser (Nanosystems and Technologies GmbH, Model S/N: 2341/13-17) with an output optical power of 3.8 mW was employed as the excitation source. The CO_2 simulated spectra within this laser's wavelength range are shown in Figure 2a, according to the HITRAN database.[32] As the water content of human skin respiration is ∼4% and the CO_2 concentration in the environmental background is ∼400 ppm, the absorption lines of 4% water and 500 ppm CO_2 were simulated simultaneously by using long-path absorption simulation. It can be seen from the figure that the absorption

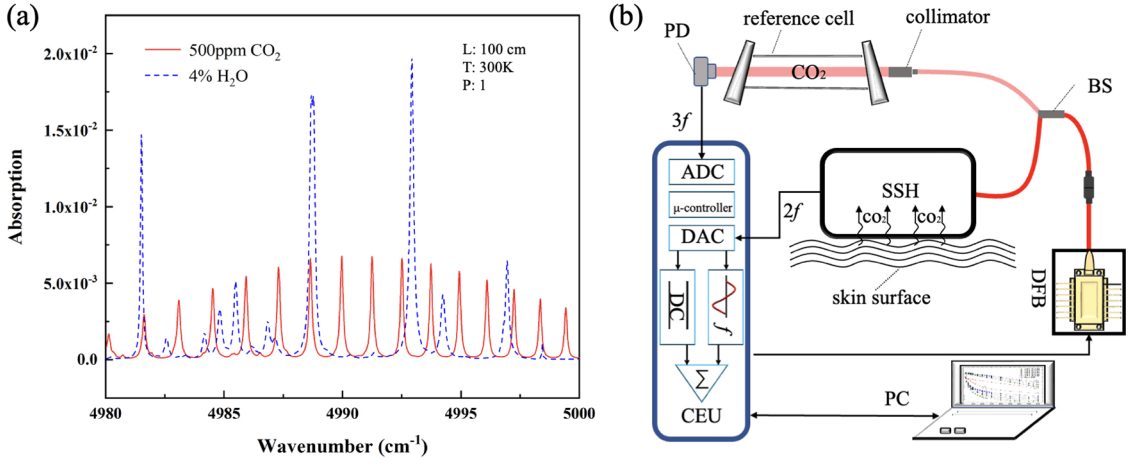

Figure 2. (a) Simulated absorption spectra of 500 ppm CO_2 and 4% H_2O according to the HITRAN database. (b) Schematic diagram of the skin respiration sensor. PD: photodetector; CEU: control electronics unit; PC: a personal computer; DFB: distributed feedback laser; and BS: 1:99 beam splitter.

https://doi.org/10.1021/acs.analchem.3c00536
Anal. Chem. 2023, 95, 6138−6144

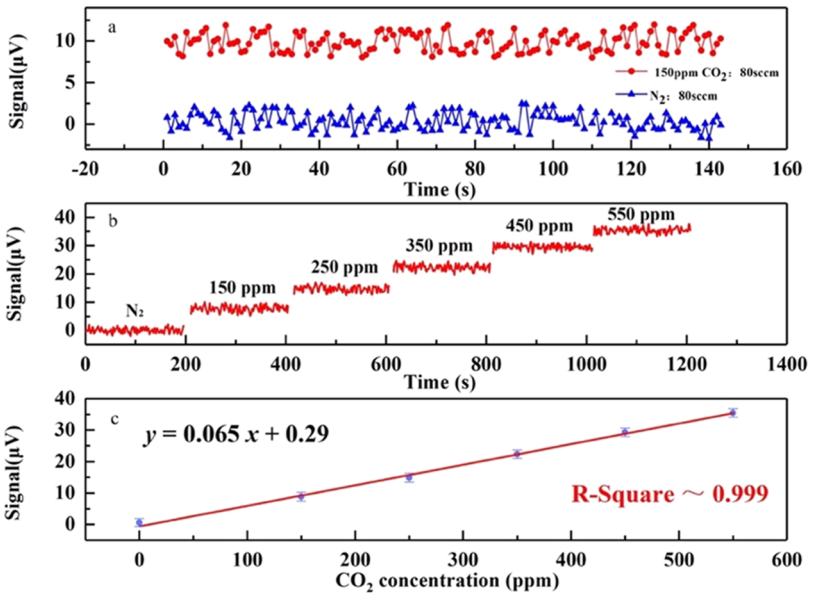

Figure 3. (a) Signal amplitude of 150 ppm CO_2/N_2 mixture (red curve) and noise level of pure N_2 (blue curve). (b) Sensor signal amplitude was repetitively recorded while the CO_2 concentration was varied. (c) The same data were averaged and plotted as a function of CO_2 concentration.

line at 4989.967 cm^{-1} is an interference-free line, so it was selected as the target line.

For a few square centimeters of skin, its elimination rate of CO_2 is ~10 ppm/min. Considering the atmospheric background, the skin respiration measurement should meet the following requirements: (1) The measured concentration range is from hundreds to thousands of ppm; (2) the measurement accuracy is ~10 ppm; (3) the measured temperature should be 37° of human body temperature and the humidity should be 3−4%. The details of the experimental setup are shown in Figure 2b. The laser was installed in a control electronics unit (CEU). The CEU was responsible for controlling laser temperature and current, locking the laser wavelength, correcting QTF frequency, and measuring signals. The laser output was split into two parts by a 1:99 fiber-optic beam splitter. 99% of the light went to the SSH. After passing through the AMR and the prong gap, the remaining laser power was 3.7 mW. 1% went to a sealed reference cell and was then detected by a photodetector. The signal from the photodetector was sent to a lock-in unit in the CEU and then demodulated at 3*f*. A 3*f* wavelength locking was applied to ensure that the laser's wavelength was always on the target absorption line. The electrical signals from the QTF were introduced into another lock-in unit in the CEU and then demodulated at 2*f*. A laptop running a LabVIEW program was used for data processing and display.

RESULTS AND DISCUSSION

Performance Assessment of Skin Respiration Sensor. The signal and noise of the skin respiration sensor based on QEPAS were first analyzed. It has been verified by a large number of experiments that the QEPAS noise is dominated by thermal noise,[33−35] which can be expressed as

$$\sqrt{V_{rms}^2} = R_g \sqrt{\frac{4K_B T}{R}} \sqrt{\Delta f} \quad (1)$$

where $\sqrt{V_{rms}^2}$ is the rms voltage of the noise, R_g is the value of the feedback resistor in the preamplifier, K_B is the Boltzmann constant, T is the QTF temperature, Δf is the system detection bandwidth, and R is the QTF equivalent resistance that is expressed as $R = Q^{-1}\sqrt{\frac{L}{C}}$, where L is the inductance in the QTF electrical parameter and C is the inverse force constant. The electrical parameters R and Q of the QTF can be measured using the CEU (R = 278.2 kΩ, Q = 6070). The time constant of the lock-in amplifier was 300 ms, corresponding to a detection bandwidth of Δf = 0.833 Hz. Therefore, the theoretical thermal noise was calculated to be 2.26 μV.

For the performance assessment, the SSH was placed in a small air chamber, which was filled with a 150 ppm CO_2/N_2 mixture at a gas flow rate of 80 sccm. The measurements were performed at atmospheric pressure and a humidifier was used to add 2.5% water to the CO_2/N_2 mixture. Figure 3a depicts the signal amplitude and the noise level. The signal-to-noise ratio is 11.65 with the 150 ppm CO_2/N_2 mixture, corresponding to a minimum detection sensitivity of 12.8 ppm. The normalized noise equivalent absorption (NNEA) coefficient was calculated to be 6.15×10^{-9} W $cm^{-1}\sqrt{Hz}$.

The sensor linearity was verified by measuring the response of the sensor to the changing CO_2 concentrations from 0 to 550 ppm. Figure 3b shows the results of repetitive measurements made every 1 s. The scatter of consecutive measurements at a certain concentration level did not depend on the concentration and agreed with the theoretical thermal noise. The plot in Figure 3c is a representation of the same measurements after all readings from each concentration step are averaged. This plot confirms the linearity of the sensor response to concentration.

The long-term stability of the skin respiration sensor was assessed by an Allen−Werle deviation analysis. The laser wavelength was locked to the CO_2 absorption line at 4989.97 cm^{-1}, and the SSH was filled with pure N_2. An acquisition time of 1 s was used to record more than 10 000 points continuously at room temperature and atmospheric pressure. The obtained analysis chart is shown in Figure 4, and the minimum detection limit reaches 35 ppb at the optimal integration time of ~670 s.

https://doi.org/10.1021/acs.analchem.3c00536
Anal. Chem. 2023, 95, 6138−6144

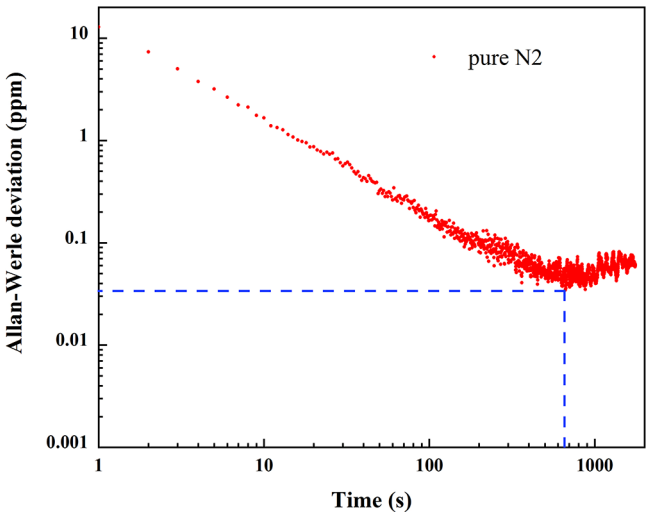

Figure 4. Allan−Werle deviation as a function of the data averaging period.

Effect of Water Vapor on the Measurement Result. Since there are sweat glands on human skin, the effect of water vapor on the vibration−translation (V−T) energy transfer rate of CO_2 molecules has to be taken into account. The CO_2 molecule has a relatively slow relaxation rate, and the addition of water greatly accelerates its V−T relaxation rate, which can be explained by the strong dipole moment of the water molecules. A 1% CO_2/N_2 mixture with changing water concentrations is filled into the system to study the effect of water vapor on the sensor signal. Figure 5 shows the signal

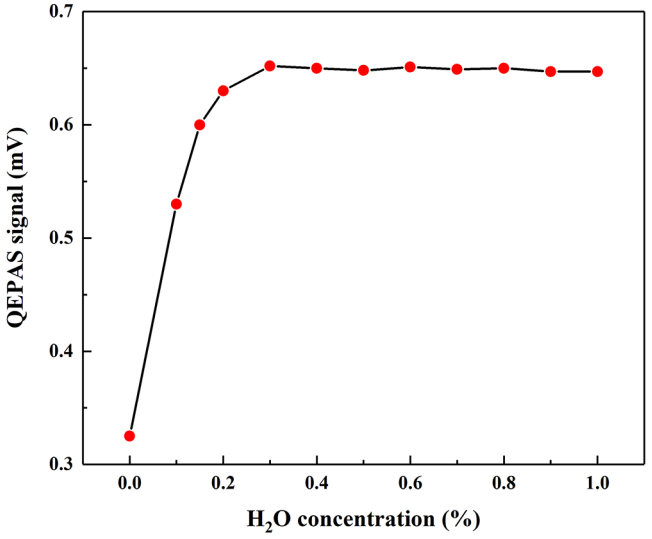

Figure 5. Signal amplitude of 1% CO_2 as a function of H_2O concentration.

curve of the skin respiration sensor as a function of H_2O concentration. The results show that the sensor's signal amplitude initially increases with the concentration level of water vapor. But when the concentration levels of water vapor are larger than 0.3%, the signal amplitude reaches a steady value, which means a higher concentration level of water vapor does not influence the sensor signal anymore. Since the concentration levels of water vapor from the environment and sweat glands are far above 0.3%, the effect of water vapor on the measurement result is not considered in the following experiment.

Static Skin Respiration Measurement. The human skin continues to eliminate CO_2 due to the presence of some blood vessels and tissues under the skin. CO_2 comes mainly from the metabolism of tissue cells (consume oxygen and produce CO_2) and lungs. CO_2 from the lungs enters the veins through the alveoli, then passes through the blood wall and tissue space, and disperses through the skin layer by layer, as shown in Figure 6. Moreover, in a healthy body, the diffusion resistance

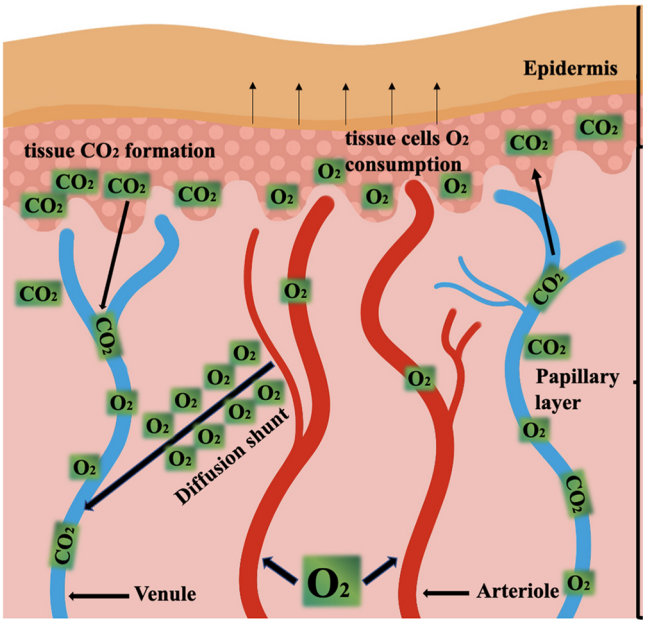

Figure 6. Sources of subcutaneous CO_2.

of CO_2 through the epidermal tissue is weak and is considered constant. But the blood flow rate in blood vessels under the skin and the metabolic rate in the epidermis can make a difference. The experiment to verify skin respiration was carried out first. CO_2 was measured from the skin surface of a subject's forearm using the skin respiration sensor, as shown in Figure 7a. Before this experiment, the subject was instructed to keep his arm flat, and a little vacuum grease was applied to the joint between the SSH and the skin so that the SSH silicon cover had good air tightness. The CO_2 concentration variation over time is shown in Figure 7b. The background concentration of CO_2 in the environment was also monitored with an additional CO_2 sensor. In 25 min, the CO_2 concentration signal levels increased from 680 ppm (environmental background) to 1120 ppm. The amount of CO_2 eliminated from the skin was up to 440 ppm. Since the change in CO_2 concentration is small, the pressure change can be negligible.

Since the CO_2 background concentrations, especially indoors, are not a constant value and may vary, it is crucial to check if this has an impact on the skin respiration measurement results. Hence, the initial CO_2 concentrations in the SSH were set to five different values successively: 32, 300, 680, 1600, and 680 ppm. After each set, the skin respiration of the same subject's forearm was measured for 10 min. The results of the five experiments with different initial CO_2 concentrations are depicted in Figure 8, which indicates that all five lines have the same slope of 10 ppm/min, regardless of

https://doi.org/10.1021/acs.analchem.3c00536
Anal. Chem. 2023, 95, 6138−6144

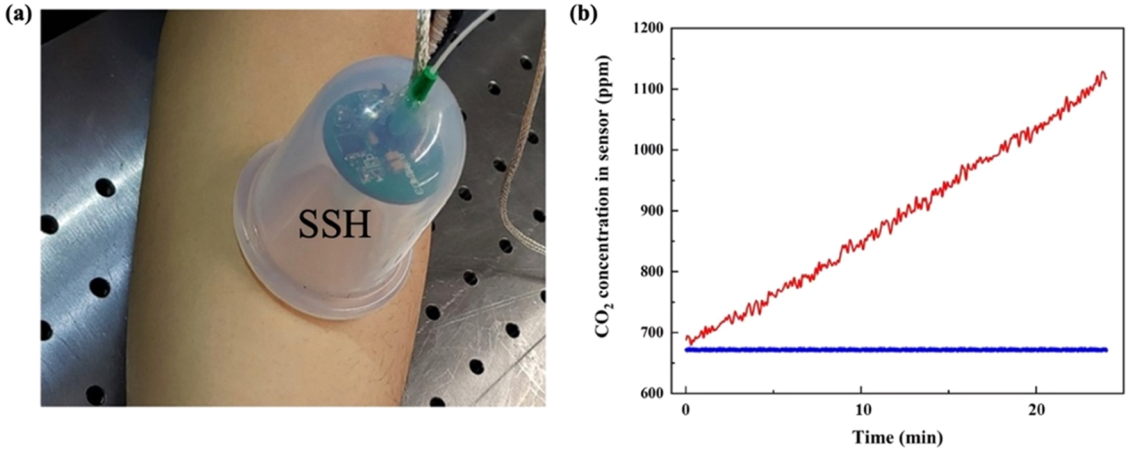

Figure 7. (a) Photograph of static skin respiration measurement. (b) Response signal of the skin respiration sensor (red line) and CO_2 background concentration (blue line).

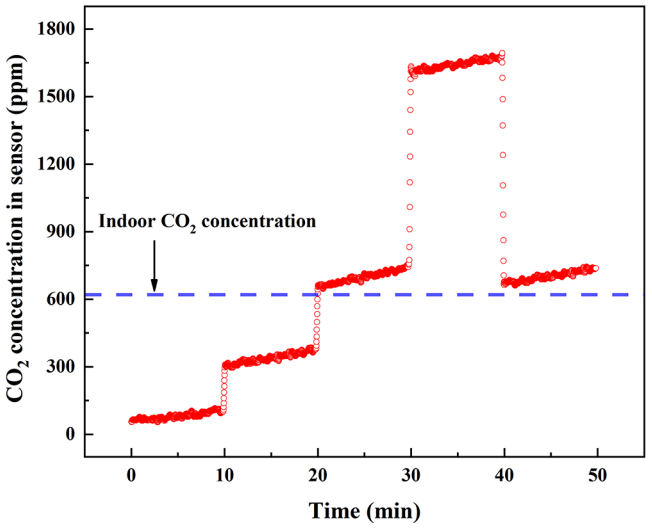

Figure 8. Static skin respiration measurement with five different initial CO_2 concentrations in the SSH.

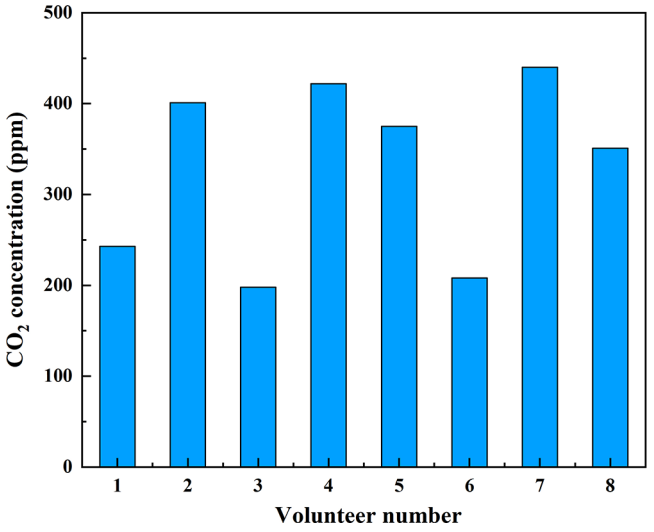

Figure 9. Amount of CO_2 eliminated from the skins of eight volunteers over 20 min.

the initial CO_2 concentrations in the SSH. Therefore, the initial CO_2 concentration in the SSH was not taken into account in the following experiments.

The elimination rate is defined as the amount of gas released per unit area per unit of time. To compare the CO_2 elimination rates of different subjects' skins, eight healthy volunteers had their skin respiration measured. Before the experiment, the volunteers tried not to change their habits for 1 day, such as their emotional state and sleep schedule. The SSH was placed on every volunteer's forearm and measured for 20 min. The results are displayed in Figure 9. The maximum CO_2 elimination rate is 2.6 ppm/min cm^2 considering the skin area of 8.5 cm^2 covered by the SSH, while the minimum rate is 1.1 ppm/min cm^2. There are significant deviations between individuals due to differences in metabolic rates and skin conditions, such as stratum corneum.

Measurement of the CO_2 elimination rate of the skin. An experiment was carried out using the skin respiration sensor to study the relationship between human motion and the CO_2 elimination rates of the skin. In theory, the skin eliminates CO_2 at a faster elimination rate when one is in motion. This is due to the fact that the amount of CO_2 in the blood and the blood flow speed increase. In this experiment, there are three volunteers involved, each weighing ~65 kg. And an elliptical machine in a well-ventilated room was employed as an exercise tool. The skin surface of the subject's forearm was cleaned with medicinal alcohol, and a little vacuum grease was applied to the skin to improve air tightness. The SSH was attached to the volunteers' forearms using a strap, as shown in Figure 10. The elliptical machine has three different tension levels. The three volunteers were allowed to choose their preferred tension level. Once selected, it cannot be changed during the experiment. A laptop running a LabVIEW program was used to collect data and calculate the CO_2 elimination rate of skin every 3 min. The experimental results are depicted in Figure 11a. For the first 10 min, the CO_2 elimination rate was constant since the volunteers had not started exercising yet. The volunteers exercised continuously for periods of 10−40, 50−80, and 90−120 min, respectively, and rested at other times (pink areas). In each exercise period, the CO_2 elimination rate rises and eventually exceeds 4 ppm/min cm^2 at 120 min. On the contrary, in each resting period, the CO_2 elimination rate gradually decreases but still maintains a high level, since it takes time for the body to recover.

https://doi.org/10.1021/acs.analchem.3c00536
Anal. Chem. 2023, 95, 6138−6144

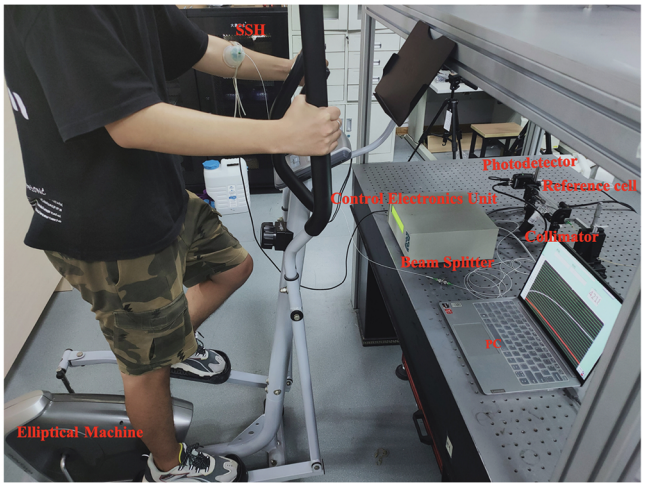

Figure 10. CO_2 elimination rate of the volunteer's skin is measured using the skin respiration sensor.

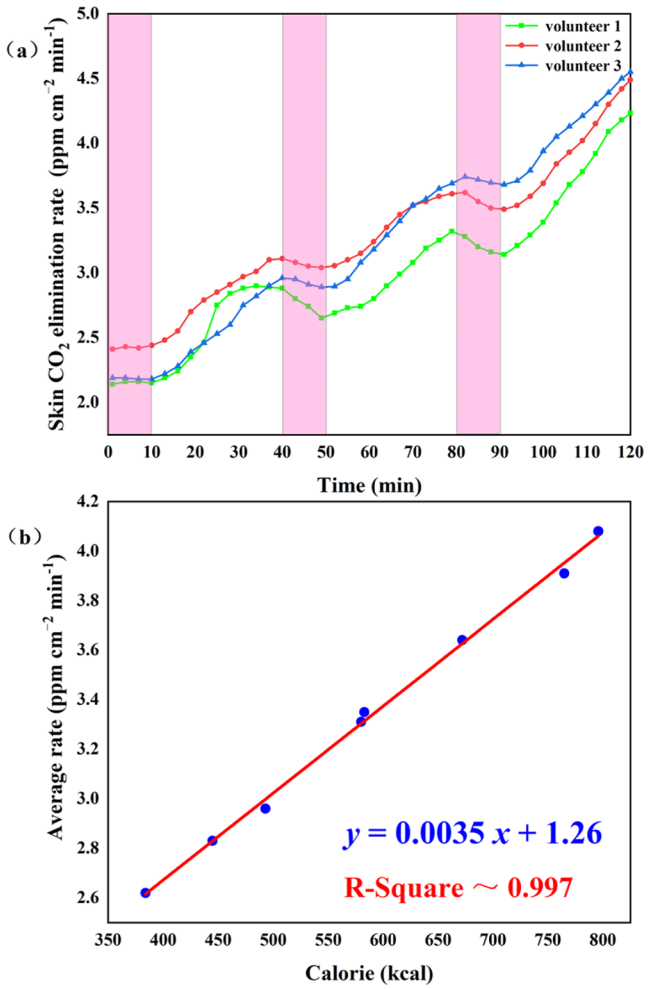

Figure 11. (a) CO_2 elimination rates of three volunteers' skin. (b) CO_2 elimination rate as a function of calorie consumption.

Due to individual differences and the intensity of exercise, each volunteer has a different average elimination rate at the same time. A variable, calorie, is introduced to characterize the relationship between the amount of exercise and the CO_2 average elimination rate. Calories are calculated using the following equation

$$\text{kcal} = w \times h \times K \quad (2)$$

where w is the weight of the volunteer, h is the exercise time, and K is a coefficient proportional to the metabolic equivalent of energy (MET, 1MET = 3.5 mL O_2/kg·min). The calorie value can be directly obtained from the display of the elliptical machine. The CO_2 average elimination rate as a function of calorie consumption is plotted in Figure 11b, which indicates excellent linearity.

CONCLUSIONS

A portable QEPAS gas sensor for the measurement of CO_2 eliminated from human skin was realized and evaluated. A minimum detection limit of 12.8 ppm was achieved at an integrated time of 300 ms, corresponding to an NNEA of 6.15×10^{-9} W cm$^{-1}\sqrt{\text{Hz}}$. The stability of the sensor is assessed by Allen−Werle deviation analysis. The minimum detection limit can be further reduced to 35 ppb at the optimal integration time of ∼670 s. The developed skin respiration sensor has the advantages of low cost, rapid response, high sensitivity, and no skin irritation. In the current medical environment, a noninvasive method of disease detection that does not necessitate complex specialized laboratory facilities and chemical reagents is particularly appealing. Sensing technologies that simultaneously identify and quantify skin-excluded CO_2 have the potential to provide noninvasive screening for hypercapnia and hypocapnia and offer early detection in critical patient situations. In the near future, the skin respiration sensor will be deployed in hospitals, where a side-by-side comparison between the TCM and this sensor will be performed through field testing among patients.

AUTHOR INFORMATION

Corresponding Author

Lei Dong − *State Key Laboratory of Quantum Optics and Quantum Optics Devices, Institute of Laser Spectroscopy, Shanxi University, Taiyuan 030006, China; Collaborative Innovation Center of Extreme Optics, Shanxi University, Taiyuan 030006, China;* orcid.org/0000-0001-7379-3388; Email: donglei@sxu.edu.cn

Authors

Biao Li − *State Key Laboratory of Quantum Optics and Quantum Optics Devices, Institute of Laser Spectroscopy, Shanxi University, Taiyuan 030006, China; Collaborative Innovation Center of Extreme Optics, Shanxi University, Taiyuan 030006, China*

Hongpeng Wu − *State Key Laboratory of Quantum Optics and Quantum Optics Devices, Institute of Laser Spectroscopy, Shanxi University, Taiyuan 030006, China; Collaborative Innovation Center of Extreme Optics, Shanxi University, Taiyuan 030006, China*

Chaofan Feng − *State Key Laboratory of Quantum Optics and Quantum Optics Devices, Institute of Laser Spectroscopy, Shanxi University, Taiyuan 030006, China; Collaborative Innovation Center of Extreme Optics, Shanxi University, Taiyuan 030006, China*

Suotang Jia − *State Key Laboratory of Quantum Optics and Quantum Optics Devices, Institute of Laser Spectroscopy, Shanxi University, Taiyuan 030006, China; Collaborative Innovation Center of Extreme Optics, Shanxi University, Taiyuan 030006, China*

Complete contact information is available at:

https://doi.org/10.1021/acs.analchem.3c00536
Anal. Chem. 2023, 95, 6138−6144

https://pubs.acs.org/10.1021/acs.analchem.3c00536

Author Contributions

§B.L. and H.W. have contributed equally to this work. All authors have given approval for the final version of the manuscript.

Notes

The authors declare no competing financial interest.

■ ACKNOWLEDGMENTS

The project was sponsored by National Key R&D Program of China (no. 2019YFE0118200); National Natural Science Foundation of China (NSFC) (nos. 62235010, 62175137, 62122045, 62075119); The Shanxi Science Fund for Distinguished Young Scholars (20210302121003); and The Open Fund of the State Key Laboratory of Integrated Optoelectronics, China (no. IOSKL2020KF10).

■ REFERENCES

(1) Arakawa, T.; Suzuki, T.; Tsujii, M.; Iitani, K.; Chien, P. J.; Ye, M.; Toma, K.; Iwasaki, Y.; Mitsubayashi, K. *Biosens. Bioelectron.* **2019**, *129*, 245−253.
(2) Gallagher, M.; Wysocki, C. J.; Leyden, J. J.; Spielman, A. I.; Sun, X.; Preti, G. *Br. J. Dermatol.* **2008**, *159*, 780−791.
(3) Di Natale, C.; Paolesse, R.; Martinelli, E.; Capuano, R. *Anal. Chim. Acta* **2014**, *824*, 1−7.
(4) Arakawa, T.; Sato, T.; Iitani, K.; Toma, K.; Mitsubayashi, K. *Anal. Chem.* **2017**, *89*, 4495−4501.
(5) Gerlach, V. *Arch. Anat. Physiol.* **1851**, 431−479.
(6) Shaw, L. A.; Messer, A. C.; Weiss, S. *Am. J. Physiol.* **1929**, *90*, 107−118.
(7) Tobias, J. D. *Pediatr. Anesth.* **2009**, *19*, 434−444.
(8) Erickson, S. J.; Grauaug, A.; Gurrin, L.; Swaminathan, M. *J. Paediatr. Child Health* **2002**, *38*, 560−562.
(9) Murase, M.; Ishida, A. *Acta Paediatr.* **2005**, *94*, 85−91.
(10) Spelten, O.; Fiedler, F.; Schier, R.; Wetsch, W. A.; Hinkelbein, J. *J. Clin. Monit. Comput.* **2017**, *31*, 153−158.
(11) Hill, K. M.; Klein, D. G. *Crit. Care Nurs. Clin. North Am.* **2006**, *18*, 211−215.
(12) Drysdale, D. *Oral Health Dent. Manage.* **2014**, *13*, 453.
(13) Geis, S.; Babilas, P.; Schreml, S.; Angele, P.; Nerlich, M.; Jung, E. M.; Prantl, L. *Clin. Hemorheol. Microcirc.* **2008**, *40*, 249−258.
(14) Stücker, M.; Struk, A.; Altmeyer, P.; Herde, M.; Baumgartl, H.; Lubbers, D. W. *J. Physiol.* **2002**, *538*, 985−994.
(15) Li, Z.; Navarro-Alvarez, N.; Keeley, E. J.; Nowell, N. H.; Goncalves, B. M. M.; Huang, C. A.; Evans, C. L. *Biomed. Opt. Express* **2017**, *8*, 4640−4651.
(16) Wu, H.; Sampaolo, A.; Dong, L.; Patimisco, P.; Liu, X.; Zheng, H.; Yin, X.; Ma, W.; Zhang, L.; Yin, W.; Spagnolo, V.; Jia, S.; Tittel, F. K. *Appl. Phys. Lett.* **2015**, *107*, No. 111104.
(17) de Cumis, M. S.; Viciam, B.; Patimisco, P.; Sampaolo, A.; Scamarcio, G.; Narale, P. D.; Amato, F. D.; Spagnolo, V. *Opt. Express* **2014**, *22*, 28222−28231.
(18) Pan, Y.; Dong, L.; Yin, X.; Wu, H. *Molecules* **2020**, *25*, 1201.
(19) Kosterev, A. A.; Bakhirkin, Yu. A.; Curl, R. F.; Tittel, F. K. *Opt. Lett.* **2002**, *27*, 1902−1904.
(20) Wu, H.; Dong, L.; Zheng, H.; Yu, Y.; Ma, W.; Zhang, L.; Yin, W.; Jia, S.; Xiao, L.; Tittel, F. K. *Nat. Commun.* **2017**, *8*, No. 15331.
(21) Yin, X.; Su, Y.; Xi, T.; Chen, B.; Zhang, L.; Zhang, X.; Liu, L.; Shao, X. *J. Appl. Phys.* **2022**, *131*, No. 130701.
(22) Liu, K.; Yi, H.; Kosterev, A. A.; Chen, W.; Dong, L.; Wang, L.; Tan, T.; Zhang, W.; Tittel, F. K.; Gao, X. *Rev. Sci. Instrum.* **2010**, *81*, No. 103103.
(23) Borri, S.; Patimisco, P.; Sampaolo, A.; Beere, H. E.; Ritchie, D. A.; Vitiello, M. S.; Sca-marcio, G.; Spagnolo, V. *Appl. Phys. Lett.* **2013**, *103*, No. 021105.
(24) Spagnolo, V.; Patimisco, P.; Borri, S.; Scamarcio, G.; Bernacki, B. E.; Kriesel, J. *Opt. Lett.* **2012**, *37*, 4461−4463.
(25) Ma, Y.; Hu, Y.; Qiao, S.; Lang, Z.; Liu, X.; He, Y.; Spagnolo, V. *Photoacoustics* **2022**, *25*, No. 100329.
(26) Lin, H.; Zheng, H.; Montano, B. Y. A. Z.; Wu, H.; Giglio, M.; Sampaolo, A.; Patimisco, P.; Zhu, W.; Zhong, Y.; Dong, L.; Kan, R.; Yu, J.; Spagnolo, V. *Photoacoustics* **2022**, *25*, No. 100321.
(27) Chen, K.; Zhang, B.; Guo, M.; Chen, Y.; Deng, H.; Yang, B.; Liu, S.; Ma, F.; Zhu, F.; Gong, Z.; Yu, Q. *Sens. Actuators, B* **2020**, *310*, No. 127825.
(28) Wei, T.; Zifarelli, A.; Russo, S. D.; Wu, H.; Menduni, G.; Patimisco, P.; Sampaolo, A.; Spagnolo, V.; Dong, L. *Appl. Phys. Rev.* **2021**, *8*, No. 041409.
(29) Zheng, K.; Zheng, C.; Ma, N.; Liu, Z.; Yang, Y.; Zhang, Y.; Wang, Y.; Tittel, F. K. *ACS Sens.* **2019**, *4*, 1899−1908.
(30) Wang, Z.; Wang, Q.; Ching, J. Y. L.; Wu, J.; Zhang, G.; Ren, W. *Sens. Actuators, B* **2017**, *246*, 710−715.
(31) Dong, L.; Kosterev, A. A.; Thomazy, D.; Tittel, F. K. *Appl. Phys. B* **2010**, *100*, 627−635.
(32) Rothman, L. S.; Rinsland, C. P.; Goldman, A.; Massie, S. T.; Edwards, D. P.; Flaud, J-M.; Perrin, A.; Camy-Peyret, C.; Dana, V.; Mandin, J.-Y.; Schroeder, J.; Mccann, A.; Gamache, R. R.; Wattson, R. B.; Yoshno, K.; Chance, K. V.; Jucks, K. W.; Brown, L. T.; Varranasi, P. *J. Quantum Spectrosc. Radiat. Transfer* **2010**, *111*, 1568−1613.
(33) Kosterev, A. A.; Tittel, F. K. *Appl. Opt.* **2004**, *43*, 6213−6217.
(34) Kosterev, A. A.; Buerki, P. R.; Dong, L.; Reed, M. D. T.; Day, T.; Tittel, F. K. *Appl. Phys. B* **2010**, *100*, 173−180.
(35) Kosterev, A. A.; Tittel, F. K.; Serebryakov, D. V.; Malinovsky, A. L.; Morozov, I. V. *Rev. Sci. Instrum.* **2005**, *76*, No. 043105.